In Vivo Transcranial Acoustoelectric Brain Imaging of Different Steady-State Visual Stimulation Paradigms

Xizi Song, *Member, IEEE*, Xiuli Su, Xinrui Chen, Minpeng Xu, *Senior Member, IEEE*, and Dong Ming, *Senior Member, IEEE*

***Abstract*— *Objective*: Based on the acoustoelectric (AE) effect, transcranial acoustoelectric brain imaging (tABI) is of potential for brain functional imaging with high temporal and spatial resolution. With nonlinear and non-steady-state, brain electrical signal is microvolt level which makes the development of tABI more difficult. This study demonstrates for the first time in vivo tABI of different steady-state visual stimulation paradigms. *Method*: To obtain different brain activation maps, we designed three steady-state visual stimulation paradigms, including binocular, left eye and right eye stimulations. Then, tABI was implemented with one fixed recording electrode. And, based on decoded signal power spectrum (tABI-power) and correlation coefficient between steady-state visual evoked potential (SSVEP) and decoded signal (tABI-cc) respectively, two imaging methods were investigated. To quantitatively evaluate tABI spatial resolution performance, ECoG was implemented at the same time. Finally, we explored the performance of tABI transient imaging. *Results*: Decoded AE signal of activation region is consistent with SSVEP in both time and frequency domains, while that of the nonactivated region is noise. Besides, with transcranial measurement, tABI has a millimeter-level spatial resolution (<3mm). Meanwhile, it can achieve millisecond-level (125ms) transient brain activity imaging. *Conclusion*: Experiment results validate tABI can realize brain functional imaging under complex paradigms and is expected to develop into a brain functional imaging method with high spatiotemporal resolution.**

***Index Terms*— Brain function imaging, different visual stimulation paradigms, high spatiotemporal resolution, steady-state visual evoked potential, transcranial acoustoelectric brain imaging.**

Manuscript received 7 April 2022; revised 4 July 2022; accepted 31 July 2022. Date of publication 5 August 2022; date of current version 12 August 2022. This work was supported in part by the National Natural Science Foundation of China under Grant 81801787, Grant 81925020, and Grant 81630051; in part by the Open Fund of State Key Laboratory of Acoustics under Grant SKLA202111; and in part by the China Postdoctoral Science Foundation under Grant 2018M640238. *(Corresponding author: Dong Ming.)*

Xizi Song, Xiuli Su, and Xinrui Chen are with the Academy of Medical Engineering and Translation Medicine, Tianjin University, Tianjin 300072, China.

Minpeng Xu is with the Department of Biomedical Engineering, College of Precision Instruments and Optoelectronics Engineering, Tianjin University, Tianjin 300072, China.

Dong Ming is with the Department of Biomedical Engineering, College of Precision Instruments and Optoelectronics Engineering, Academy of Medical Engineering and Translation Medicine, Tianjin University, Tianjin 300072, China (e-mail: richardming@tju.edu.cn).

Digital Object Identifier 10.1109/TNSRE.2022.3196828

I. Introduction

BRAIN functional imaging is an effective technology to non-invasively detect the changes in structure and function of the brain, which is important for the diagnosis and treatment of brain disorders. A variety of brain function imaging approaches have been developed to understand dynamic brain activity, including functional magnetic resonance imaging (fMRI), electroencephalography (EEG), functional near-infrared spectroscopy (fNIRS), etc. fMRI provides an excellent spatial resolution (∼mm) but has slow dynamics (∼s) to image brain activity [1]. EEG offers a fine temporal resolution (∼ms), yet has limited spatial resolution (∼cm) due to the effect of the volume conductor [2]. As the single modal imaging approaches can't have a high temporal or spatial resolution, multimodalities have been presented, such as fNIRS-EEG and fMRI-EEG [3], [4]. While the combination of two complementary modalities can get more accurate and reliable brain information, the asynchronous data types impose a formidable task for data fusion timely [5]. The latest transcranial Acoustoelectric Brain Imaging (tABI) offers a novel way to map electrical activity in the brain [6]. This approach decodes brain activities by measuring acoustoelectric (AE) signals in the ultrasound focus volume using EEG. Due to the spatial focality of focused ultrasound (FUS) and the good temporal resolution of EEG, tABI is a potential brain functional imaging approach with high spatiotemporal resolution.

The AE effect is the local conductivity change produced by the propagation of ultrasound in the medium. It was first discovered by Fox [7], and soon others measured the signal in saline solution [8], [9]. Recently, many studies have been focusing on AE imaging. In phantom experiments, R. Olafsson *et al.* proposed a concept of ultrasound current source density imaging (UCSDI) with improved spatial resolution. It can locate a 2D current source within 1mm of its actual position [10]. Yijie *et al.* evaluated multisource AE imaging with different current source features and effectively extracted corresponding features from AE signals. They

achieved 1-2mm of the −6dB peak spatial resolution with an average SNR of 15.4dB in multisource AE imaging [11]. In biological tissue experiments, R. S. Witte *et al.* demonstrated the feasibility of accurately imaging varying current densities using AE imaging in a lobster nerve cord injected with current [12] and in an isolated paced rabbit heart [13]. Then, B. Berthon *et al.* attempted to map electrical activation in beating rat hearts with ultrafast acoustoelectric Imaging (UAI) [14]. The results proved that UAI can produce 2D images of the measured UAI signal with good spatial and temporal resolution. Alexander *et al.* demonstrated for the first time in vivo ACI with high spatial (<3mm) and temporal resolution (<1ms) in a swine model [15]. These studies have demonstrated the potential of AE imaging.

Few AE imaging studies about living brain tissue have been conducted. Because the brain signal is weak and non-linear, it makes the development of tABI more difficult. Bin He proposed that acousto-electrophysiological neuroimaging (AENI) combined FUS with electrophysiological neuroimaging. And he assumed that the recorded electromagnetic signals can demodulate the inherent brain electrical activity [16]. Then, tABI was presented by Y. Qin et al in 2017 [6], which is like AENI but more specific in electromagnetic signal type. The feasibility of using an artificial current source for AEI in a human head model and rat hippocampus has been confirmed, and many studies have shown that tABI may be able to accurately resolve deep neuron currents with a high spatial resolution (<3mm) [17], [18], [19], [20], [21]. But these models mainly use artificial current sources to simulate neural activity and lack valuable real brain data for verification and optimization. In 2021, Xizi *et al.* achieved millimeter-level spatial resolution steady-state visual evoked potential (SSVEP) measurement in living rats through ABI for the first time. The study systematically verified the feasibility of AE signal decoding brain activities of living rats in terms of timing and frequency [22].

To explore the imaging potential of tABI, this study investigates for the first time in vivo tABI of different steady-state visual stimulation paradigms. In the experiment, the recorded signal on the activated brain region was shown and decoded. And the decoded AE (decAE) signals of different brain regions were analyzed in both time and frequency domains. Besides, brain activation maps were imaged with two tABI methods and Electrocorticography (ECoG). And the spatial resolution performance of tABI and ECoG were evaluated. Finally, the performance of tABI transient imaging was explored, and tABI images within 3s, 1s and 125ms were respectively obtained with the same rat.

II. Theory

A. AE Effect

AE effect is the foundation of tABI. The propagation of ultrasound induces an acoustic pressure variation ΔP which causes a change in medium resistivity $\Delta\rho$ given by

$$\Delta\rho = K\rho_0 \Delta P \tag{1}$$

where ρ_0 is the initial medium resistivity before perturbation, K is an interaction constant. In consequence, when FUS propagates in the local medium, the resistivity is

$$\rho = \rho_0 + K\rho_0 \Delta P \tag{2}$$

B. Lead Field Theory

A lead is constructed of a pair of electrodes and its sensitivity is called a lead field. If the unit current passes through the lead, the shape and distribution of the lead field are the same as the electric field, and the voltage V_i detected by lead i can be described as

$$V_i = \int\int\int \left(\tilde{J}_i^L \cdot J^I\right) \rho dxdydz \tag{3}$$

where J^I is the current source distribution, $\tilde{J}_i^L$ is the lead field of lead i.

C. Transcranial Acoustoelectric Brain Imaging

Based on (2) and (3), when FUS propagates in the brain medium, the V_i measured by lead i can be rewritten as

$$V_i = V_i^{LF} + V_i^{AE} \tag{4}$$

$$V_i^{LF} = \int\int\int \left(\tilde{J}_i^L \cdot J^I\right) \rho_0 dxdydz \tag{5}$$

$$V_i^{AE} = \int\int\int \left(\tilde{J}_i^L \cdot J^I\right) K\rho_0 \Delta P dxdydz \tag{6}$$

where V_i^{LF} is the directly measured voltage without FUS, produced by low-frequency current source J^I, which is the traditional EEG. V_i^{AE} is the AE signal. It is of high frequency consistent with the ultrasound frequency. According to (6), the AE signal is non-zero when current source J^I is non-zero at the focal spot in brain. This means that, at the activated brain region, high-frequency AE signal would be detected, while, at the nonactivated brain region, only noise would be detected. The location of the source of the AE signal is corresponding to the known location of the focal spot of the FUS. Therefore, by scanning the brain with FUS of a millimeter precision, the brain electrical activity and the source location can be obtained from the decoded AE signal detected by the electrodes with millimeter spatial resolution.

III. Methods

A. Animals and Ethics Statement

Fifteen male Wistar rats (body weight 260-320g), named rat 1-rat 15, are used in the study. The animals are housed on a 12:12h light-dark schedule with food and water ad libitum. On the day of the experiment, the rats are anesthetized with 30% urethane (3-5ml/kg) and positioned onto a stereotaxic frame (RWD Life Science, 68044) with ear rods. To accurately locate the positions of electrodes and FUS, the scalp is quickly excised to reveal the skull. All experiments are performed in accordance with the Animal Management Rules of the Ministry of Health of the People's Republic of China. All procedures are approved by the Animal Research Ethics Committee, School of Medicine, Medical College of Tianjin University.

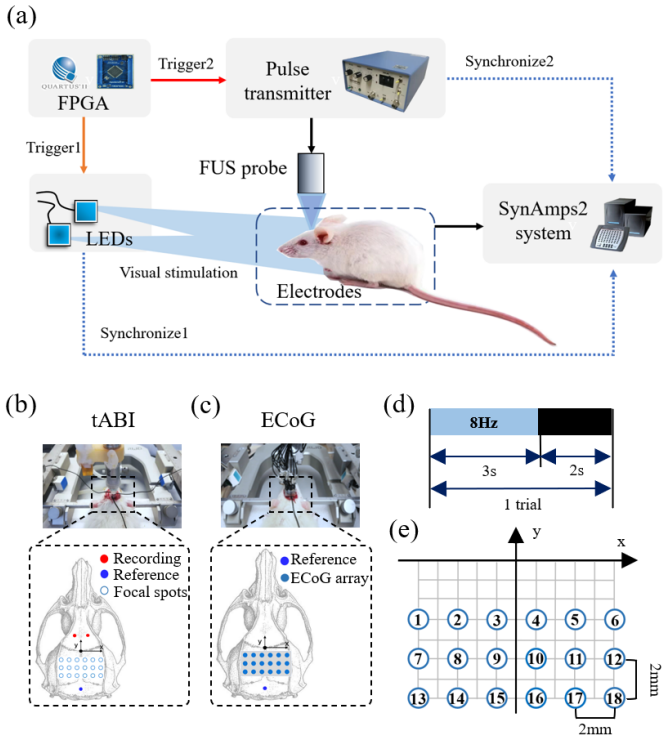

Fig. 1. (a) Schematic diagram of the experimental setup and materials. (b) The experimental scene, and the position diagram of electrodes and focal spots in the tABI experiment. (c) The experimental scene, and the position diagram of electrodes array in the ECoG experiment. (d) Schematic diagram of the visual stimulation for a trail. (e) The scanned area in the tABI experiment. Along x-direction, transducer scanned 10 mm (x = − 5−5mm), producing six focal spots totally. Along y-direction, it scanned 4mm (y = −3−7mm), generating three focal spots in total.

B. Experiment Setup

The experiment setup used in this study is shown in Fig. 1 (a). LEDs are used for steady-state visual stimulation. Marked with the orange solid arrow, the flashing time and frequency of LEDs are triggered and controlled by field programmable gate array (FPGA). Three steady-state visual stimulation paradigms are designed to obtain different SSVEP distribution in rat brain, including binocular stimulation, left eye stimulation and right eye stimulation paradigm. Under the binocular stimulation paradigm, two 15mm × 15mm blue square LEDs, simultaneously flickering at 8Hz, are placed on both sides of the rat's nose and are 10cm away from the rat's eyes. Under two monocular stimulation paradigms, one LED flickers at the stimulating side, and the LED on the non-stimulating side is removed. The eye on the non-stimulating side is coated with erythromycin eye ointment and pasted with black opaque tape to avoid light. As shown in Fig. 1 (d), there are 3s visual stimuli and 2s rest in a trial and a block contained 18 trials.

The pulse transmitter/receiver (Olympus, 5077PR, USA) drives the FUS probe (A303S, 1MHz, 20mm focal length, Olympus, USA) to produce FUS waves. Marked with the red solid arrow in Fig. 1 (a), pulse transmitter time and pulse repetition frequency (PRF) of FUS (120Hz, 0.12% duty cycle) are triggered and controlled by FPGA [22]. The size of the focal spot is 2.8mm (lateral dimensions) when ultrasound pressure decreases around 3dB. And the maximum pressure measured in water is 1.57MPa, which is safe for diagnostic imaging as previously described [19]. Controlled by a programmable stepper motor, the FUS probe scans sequentially according to the numbers displayed in Fig. 1 (e). The size of the scan area is 4mm × 10mm and the step size is 2mm. The FUS probe is fitted with a conical collimator to locate the focal spots and the conical collimator is filled with coupling agent to propagate FUS. And at each focal spot, the corresponding electrical signal is measured.

TABLE I
THE STRUCTURES OF BRIAN IMAGING REGION

Position	Abbreviation	Structure
1, 6	S1FL-S1DZ	Primary somatosensory cortex, forelimb region-Primary somatosensory cortex, dysgranular zone
2, 5	S1Tr	Primary somatosensory cortex, trunk region
3, 4	M2	Secondary motor cortex
7, 12	V2L-V1	Secondary visual cortex, lateral area-Primary visual cortex
8, 11	V2ML	Secondary visual cortex, mediolateral area
9, 10	V1mm-RSD	Secondary visual cortex, mediomedial area-Retrosplenial dysgranular cortex
13, 18	V1B	Primary visual cortex, binocular area
14, 17	V1M	primary visual cortex, monocular area
15, 16	V1mm-RSD	Secondary visual cortex, mediomedial area-Retrosplenial dysgranular cortex

Fig. 1 (b-c) displays the experimental scene photograph and electrode configuration of tABI and ECoG. For tABI, the columnar non-invasive electrodes (AgCl) are adopted to detect signals, consisting of low-frequency EEG signal and high-frequency AE signal. As shown in Fig. 1 (b), the columnar non-invasive electrodes are placed on the surface of the skull. Taking bregma as origin, the reference electrode coordinate is (0mm, −10.4mm), located on the cerebellar (Cb) region. The coordinates of the two recording electrodes are (−1mm, 4mm) and (1mm, 4mm), located on the left frontal association cortex (FrA_L) and right frontal association cortex (FrA_R). The ground electrode is fixed at the tail. For ECoG, the 18-needle electrode array (platinum) is adopted, which is shown in Fig. 1 (c). The 18 electrodes of the ECoG array are embedded in the 18 holes of the skull and the ends of the electrodes just touch the cerebral cortex. To make the imaging region the same for the two imaging modes, the electrode arrangement of the 18-electrode array is consistent with the position of 18 ultrasound focal spots. The positions of reference and ground electrodes in the ECoG experiment are the same as those in the tABI experiment. According to Paxinos and Watson [23], the structures of the brain imaging region in this experiment are listed in table I.

C. Signal Acquisition

In the tABI experiment, three rats are used under each visual stimulation paradigm. The signal of each position in imaging region is sequentially collected when FUS probe

scanning on corresponding focal spot. Under each steady-state visual stimulation paradigm, 150s (a block) signal is recorded for each focal spot. Three rats are adopted in the ECoG experiment, and each rat is used under three visual stimulation paradigms in turn. And a ten-minute rest is implemented between paradigms. With the pulse transmitter turned off and the FUS probe removed, the signal of each position in the imaging region is synchronously detected by the 18-electrode array under each steady-state visual stimulation paradigm. For each rat, to make the rat reach a similar state to the long-term visual stimulation of the tABI experiment, three blocks are recorded and averaged to one block. Besides, to better evaluate and verify the imaging accuracy of tABI, the tABI experiment and the ECoG experiment are successively implemented with the same rat under the same visual stimulation paradigm, adopting three rats under three visual stimulation paradigms. And there is about 30min operation time to place an invasive 18-needle electrode array before collecting ECoG signals.

All signals detected by electrodes are acquired, amplified, and filtered by the SynAmps2 system (Neuroscan, USA). The sampling rate is 20kHz and the bandpass filtering range is 0–3500Hz. The setup ensures fully synchronized recording of LED flickering time, pulse emission time and signal detected by electrodes. All signals in this experiment are detected in a dark environment to avoid interference from natural light.

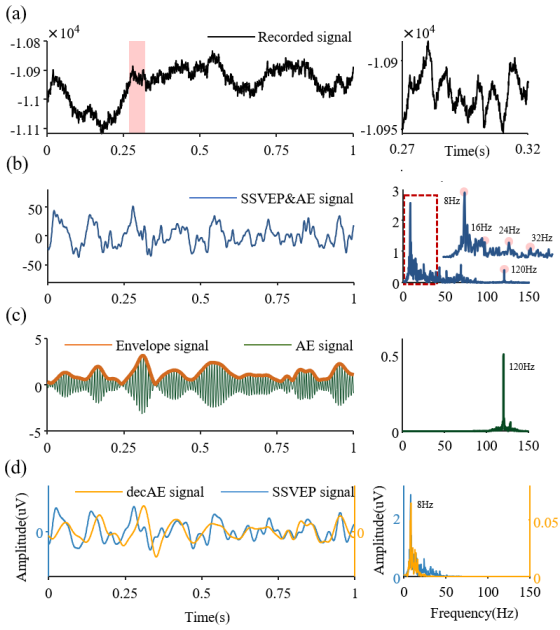

Fig. 2. (a) The 1-second recorded signal and the 5-millisecond enlarged recorded signal in pink shade. (b) The SSVEP&AE signal after down-sampling and bandpass filtering (6-150Hz). (c) The AE signal with bandpass filtering (105-135Hz) and envelope signal. (d) The SSVEP signal with bandpass filtering (6-40Hz) and decAE signal.

D. Image Processing

1) Image Processing of tABI: In the imaging of tABI, the signals of one electrode detected on FrA_L or FrA_R are used, depending on who has the better low-frequency SSVEP signal. AE signal with a higher signal-to-noise ratio can be measured based on the electrode that can measure a good SSVEP. And then decoding the high-frequency part of the signals can determine whether the focus points are the location of the SSVEP sources.

For each focal spot in tABI experiment, the recorded signal is first down-sampled at 2000Hz. Then the signal is filtered using a 6-40Hz band-pass filter to obtain SSVEP and a 105-135Hz band-pass filter to obtain the AE signal. The filtered signals in the stimulus state (3s) are intercepted and averaged across trials. The Hilbert transform is used to convert the AE signal to an analytical form whose absolute value determined the envelope of the AE signal. The same band-pass filter (6-40Hz) is also applied to the envelope of the AE signal to obtain the decAE signal. Fast Fourier transform is taken to calculate the power spectrum of decAE signal. The sum of power of decAE at base frequency (8Hz) and second harmonic frequency (16Hz) of visual stimuli frequency and the time domains correlation coefficient between decAE signal and average SSVEP of all focal spots (Ave-SSVEP) are two important values to represent the magnitude (intensity) of the local current densities. According to the known coordinate of each focal spot, the two kinds of data are converted into decibel values to form two different corresponding matrixes. Finally, the two corresponding matrixes are respectively interpolated at 0.5 interval to reconstruct tABI of power spectrum (tABI-power) and tABI of correlation coefficient (tABI-cc) on hot color map. For the tABI-cc, the correlation coefficient is calculated by

$$CC = \frac{\sum_{l=1}^{len} \left(X_l - \bar{X}\right)\left(Y_l - \bar{Y}\right)}{\sqrt{\sum_{l=1}^{len} \left(X_l - \bar{X}\right)^2 \left(Y_l - \bar{Y}\right)^2}} \tag{7}$$

where X is the Ave-SSVEP, Y is the decAE, $CC \in [-1, 1]$. If the value of CC_i at spot i is greater than zero, the decibel value of CC_i (cc_i) will be defined as

$$cc_i = 20 \times lg\left(\frac{CC_i}{max\left\{CC_1, CC_2, \ldots, CC_{18}\right\}}\right) \tag{8}$$

if the value of CC_i is less than or equal to zero, cc_i is set to the color bar minimum dB value.

2) Image Processing of ECoG: For each measuring position in ECoG experiment, the recorded signal is first down-sampled at 2000Hz. Then the signal is filtered using a 6-40Hz band-pass filter to obtain SSVEP. The filtered signals in the stimulus state are intercepted and averaged across trials. Fast Fourier transform is taken to calculate the power spectrum of SSVEP. The sum of power of SSVEP at base frequency (8Hz) and second harmonic frequency (16Hz) of visual stimuli frequency is used to reconstruct ECoG.

IV. Results

A. Analysis of Recorded Signals

With ultrasound probe focusing on the activated brain region, Fig. 2 (a) shows the recorded one trial signal of one rat (rat 7). Fig. 2 (a) displays the 1-second recorded signal, with the 0.05-second signal zoomed in. There are 6 cycles during the 0.05-second recorded signal, and the periodicity matches

the PRF of ultrasound (120Hz). After down-sampling and 6-150Hz bandpass filtering, SSVEP&AE signal is obtained, which is displayed in Fig. 2 (b). Marked with the red box in the spectrum of the SSVEP&AE signal, obvious peaks are observed at the base and harmonic frequencies of visual stimulus (8Hz). And an obvious peak also is observed at PRF of ultrasound (120Hz). With 6-40Hz bandpass filtering, the SSVEP signal is obtained, which is displayed in Fig. 2 (d). With 105-135Hz bandpass filtering, the AE signal is obtained, which is displayed in Fig. 2 (c).

With the Hilbert transform, the envelope signal, shown in Fig. 2 (c), is obtained from AE signal. Then, with a 6-40Hz bandpass filter, the filtered envelope signal is the decAE signal, which is shown in Fig. 2 (d). As exhibited in Fig. 2 (d), the decAE signal is consistent with SSVEP in both time and frequency domains. In the frequency domain, the frequency of the decAE signal is 8Hz, which is the same as that of SSVEP. Besides, the decAE signal is of the consistent phase and amplitude as the SSVEP in the time domain.

B. decAE Signal Characteristics of Different Brain Regions

Under three steady-state visual stimulation paradigms, decAE signals of different brain regions are respectively analyzed in both the time and frequency domains. The data is calculated with the average of all trials from three rats.

1) Binocular Stimulation: With recording electrode placed on FrA_L, decAE signals of different brain regions are analyzed under binocular steady-state visual stimulation paradigm. Four typical regions are discussed, including spot 2 (S1Tr), spot 5 (S1Tr), spot 14 (V1M), spot 17 (V1M). And the simultaneously measured SSVEP of all the 18 regions are averaged. For three rats (rat 1, rat 2, rat 3), the power spectrogram of decAE signals is shown in Fig. 3 (b). Obvious high powers are observed for decAE-14 and decAE-17 signals at 8Hz and 16Hz. For 8Hz and 16Hz, the sum of mean SNRs of decAE signals are calculated and shown in Fig. 3 (c). Obviously, the sum of mean SNRs of decAE signals at spot 14 and 17 are significantly higher than that at spot 2 and 5. For these four brain regions, 8 cycles (1s) of the Ave-SSVEP and decAE signals are displayed respectively in Fig. 3 (d). The decAE-14 and decAE-17 are positively correlated with Ave-SSVEP in phase and magnitude. According to the correlation analysis above the waveforms, the waveforms of decAE-14 and decAE-17 have significant correlation with Ave-SSVEP, compared to that of decAE-2 and decAE-5 (decAE-2: $r = -0.0947$, $p = 0.015$; decAE-5: $r = 0.0745$, $p = 0.014$; decAE-14: $r = 0.3798$, $p < 0.001$; decAE-17: $r = 0.5651$, $p < 0.001$). The visual cortex is activated while the somatosensory cortex is nonactivated in the experiment. Meanwhile, under binocular steady-state visual stimulation paradigm, the bilateral visual area is activated.

2) Left Eye Stimulation: With recording electrode placed on FrA_R, decAE signals of different brain regions are analyzed under left eye steady-state visual stimulation paradigm. Four typical regions are discussed, including spot 2, spot 5, spot 14, spot 17. And the simultaneously measured SSVEP of all the 18 regions are also averaged. The power spectrogram of decAE signals (rat 4, rat 5, rat 6) is shown in Fig. 4 (b). Obvious high powers are observed for decAE-17 signal at 8Hz and 16Hz. For 8Hz and 16Hz, the sum of mean SNRs of decAE signals are calculated and shown in Fig. 4 (c). And the sum of mean SNRs of decAE signals at spot 17 is significantly higher than that at spot 2, 5 and 14. Besides, according to the correlation analysis above the waveforms of Ave-SSVEP and decAE signals in Fig. 4 (d), only the decAE-17 is positively correlated with Ave-SSVEP in phase and magnitude. Compared to that of decAE-2, decAE-5 and decAE-14, the waveform of decAE-17 has a significant correlation with Ave-SSVEP (decAE-2: $r = -0.0608$, $p = 0.0065$; decAE-5: $r = 0.1152$, $p = 0.0021$; decAE-14: $r = 0.0667$, $p = 0.0029$; decAE-17: $r = 0.627$, $p < 0.001$). These experiment results validate that right visual area is activated under left eye steady-state visual stimulation paradigm.

3) Right Eye Stimulation: With recording electrode placed on FrA_R, decAE signals of different brain regions are analyzed under right eye steady-state visual stimulation paradigm. Four typical regions are discussed, including spot 2, spot 5, spot 8 (V2ML), spot 11 (V2ML). And the simultaneously measured SSVEP of all the 18 regions are also averaged. The power

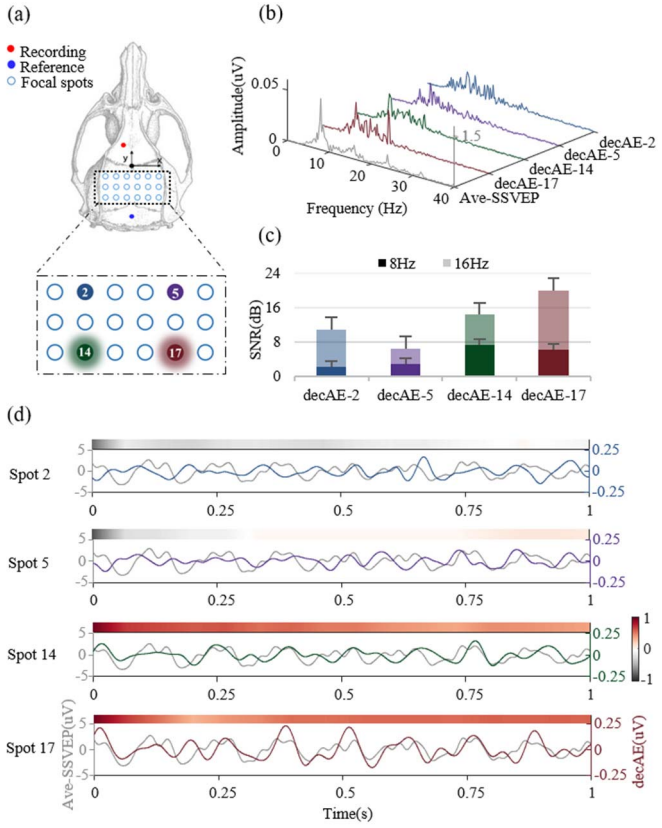

Fig. 3. Under binocular visual stimulation paradigm, decAE signal characteristics of four brain regions are analyzed. (a) Diagram of electrodes and focal spots. (b) Amplitude spectrum of Ave-SSVEP and decAE signals. (c) Sum of mean SNRs of decAE signals at 8Hz and 16Hz. (d) The waveforms of Ave-SSVEP and decAE signals. Color bar (right): Correlation coefficient reflects the significance of correlation between different signals. Color map (top): The correlation between different signals of corresponding frequency according to color bar.

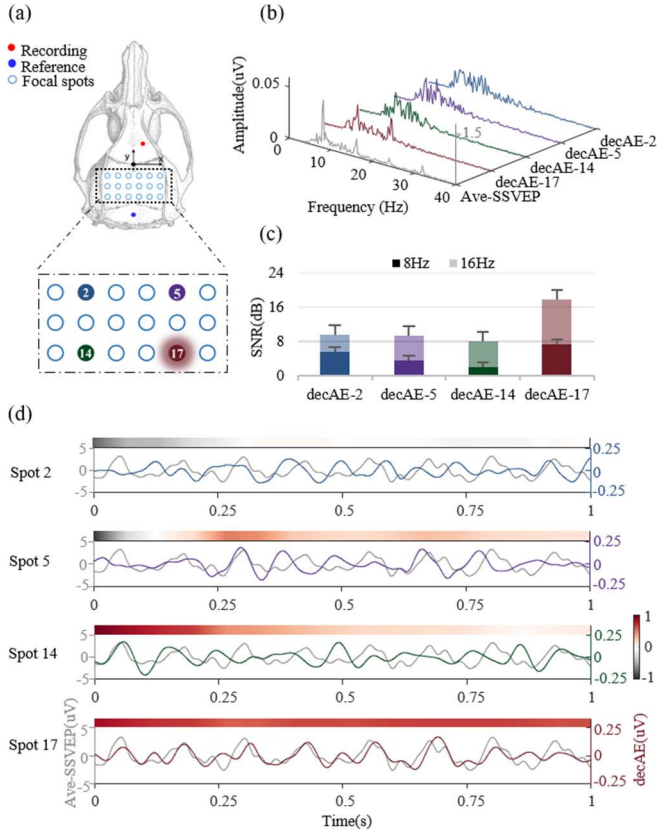

Fig. 4. Under left eye visual stimulation paradigm, decAE signal characteristics of four brain regions are analyzed. (a) Diagram of electrodes and focal spots. (b) Amplitude spectrum of Ave-SSVEP and decAE signals. (c) Sum of mean SNRs of decAE signals at 8Hz and 16Hz. (d) The waveforms of Ave-SSVEP and decAE signals. Color bar (right): Correlation coefficient reflects the significance of correlation between different signals. Color map (top): The correlation between different signals of corresponding frequency according to color bar.

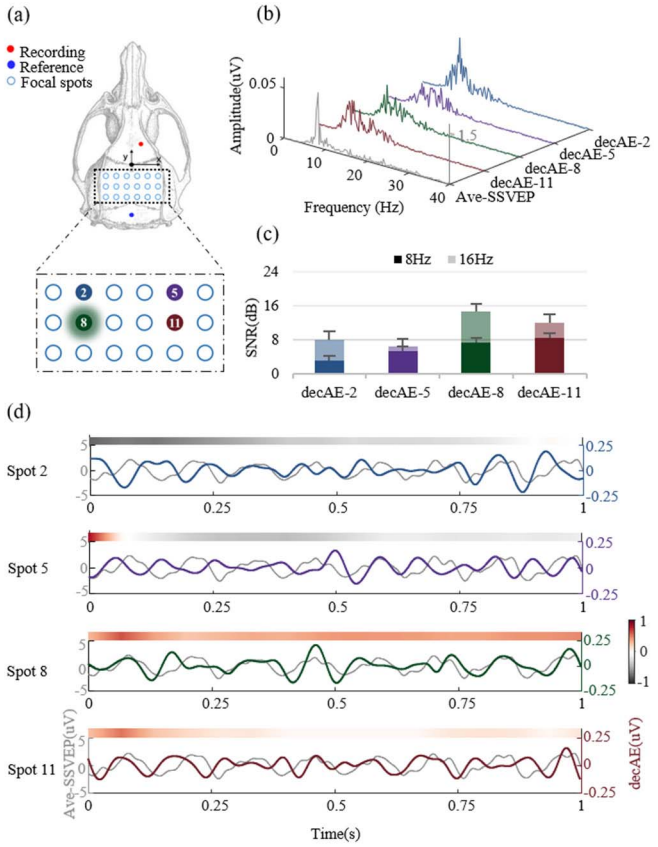

Fig. 5. Under right eye visual stimulation paradigm, decAE signal characteristics of four brain regions are analyzed. (a) Diagram of electrodes and focal spots. (b) Amplitude spectrum of Ave-SSVEP and decAE signals. (c) Sum of mean SNRs of decAE signals at 8Hz and 16Hz. (d) The waveforms of Ave-SSVEP and decAE signals. Color bar (right): Correlation coefficient reflects the significance of correlation between different signals. Color map (top): The correlation between different signals of corresponding frequency according to color bar.

spectrogram of decAE signals (rat 7, rat 8, rat 9) is shown in Fig. 5 (b). Obvious high powers are observed for decAE-8 signal at 8Hz and 16Hz. For 8Hz and 16Hz, the sum of mean SNRs of decAE signals are calculated and shown in Fig. 5 (c). And the sum of mean SNRs of decAE signals at spot 8 is significantly higher than that at spot 2, 5 and 11. Besides, according to the correlation analysis above the waveforms of Ave-SSVEP and decAE signals in Fig. 5 (d), only the decAE-8 is positively correlated with Ave-SSVEP in phase and magnitude. Compared to that of decAE-2, decAE-5 and decAE-11, the waveform of decAE-8 has a significant correlation with Ave-SSVEP (decAE-2: $r = -0.0539$, $p = 0.0159$; decAE-5: $r = -0.1421$, $p < 0.001$; decAE-8: $r = 0.4581$, $p < 0.001$; decAE-11: $r = 0.1006$, $p = 0.0164$). These experiment results validate that left visual area is activated under right eye steady-state visual stimulation paradigm.

C. Brain Activation Mapping of Different Steady-State Visual Stimulation Paradigms

To obtain the target brain activation map under different steady-state visual stimulation paradigms, the ECoG experiment (rat 10, rat 11, rat 12) is first implemented. The right

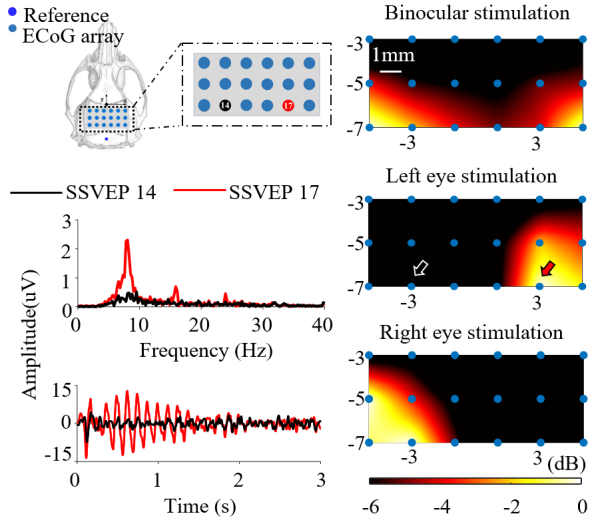

Fig. 6. The brain activation mapping of ECoG under different steady-state visual stimulation paradigms. And the SSVEP at activated and nonactivated regions under left eye visual stimulation are analyzed in both time and frequency domains.

panel of Fig. 6 shows the corresponding brain activation mapping. It can be seen that, consistent with previous study [24], bilateral brain regions are activated under binocular visual stimulation paradigm, and the contralateral brain regions

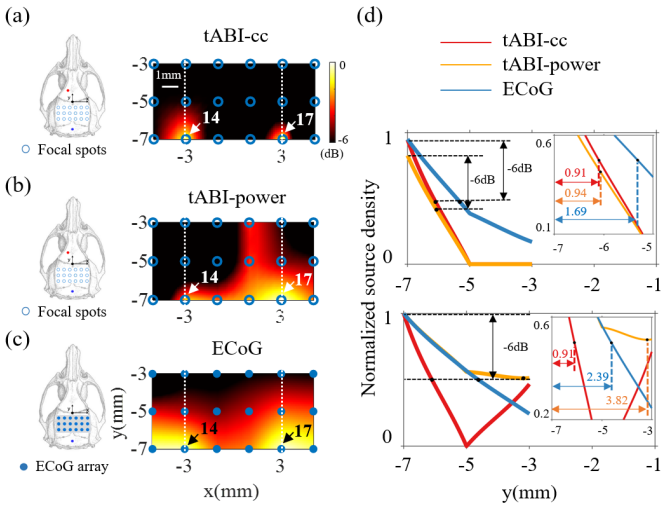

Fig. 7. Under binocular steady-state visual stimulation paradigm, (a)-(c) separately show the tABI-cc, tABI-power, ECoG for same rat. (d) show the normalized source density along the two white dashed-lines in the images.

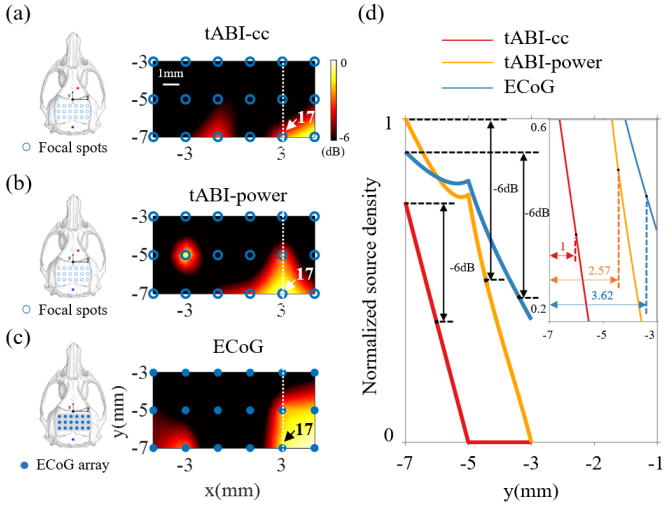

Fig. 8. Under left eye steady-state visual stimulation paradigm, (a)-(c) separately show the tABI-cc, tABI-power, ECoG for same rat. (d) show the normalized source density along the white dashed-line in the images.

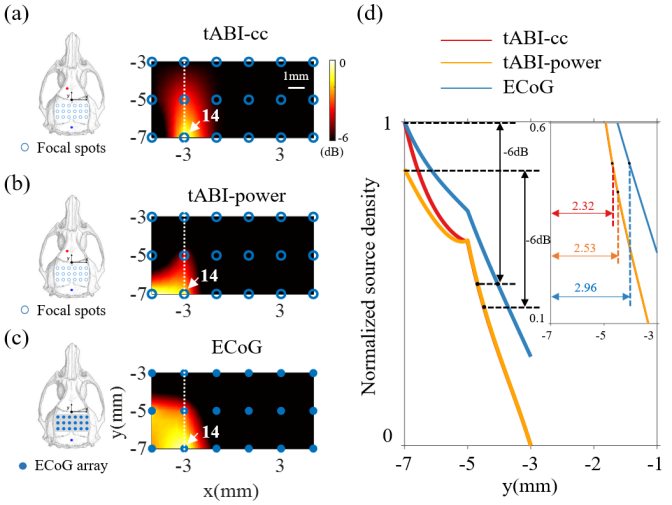

Fig. 9. Under right eye steady-state visual stimulation paradigm, (a)-(c) separately show the tABI-cc, tABI-power, ECoG for same rat. (d) show the normalized source density along the white dashed-line in the images.

are significantly activated under two monocular stimulation paradigms. In addition, under left eye visual stimulation, the SSVEP at activated and inactivated brain regions are analyzed in both time and frequency domains, which are displayed in the left panel of Fig. 6. In the spectrogram, the power of SSVEP-17 at 16Hz and 8Hz is much higher than that of SSVEP-14. And the average amplitude of SSVEP-17 within 3s is also higher than that of SSVEP-14. Those ECoG experiment results provide a reference of actual brain activation maps to test the tABI performance.

Under binocular steady-state visual stimulation paradigm, Fig. 7 shows the brain activation mappings of tABI-cc, tABI-power, and ECoG for the same rat (rat 13). First, it can be seen from Fig. 7 (a-c) that, with obvious strong signal observed at spot 14 and 17, consistent brain activation mappings are imaged with these three methods. Quantitatively, the correlation coefficient between tABI-cc and ECoG is 0.5064 ($p = 0.032$). And the correlation coefficient between tABI-power and ECoG is 0.5663 ($p = 0.0143$). In addition, the normalized source density along the two white dashed-lines in Fig. 7 (a-c) is shown in Fig. 7 (d). For tABI-cc, tABI-power and ECoG, with the same peak position (y $= -$ 7mm), the anode width of the $-$6dB peak is 0.91mm, 0.94mm and 1.69mm respectively along the left line. Along the right line, the corresponding anode width is 0.91mm, 3.82mm and 2.39mm respectively. At the same time, it needs to point out that the theories of tABI-cc and tABI-power are different. The anode widths are mainly to show the imaging result and not to compare imaging quality.

Under left eye steady-state visual stimulation paradigm, Fig. 8 shows the brain activation mappings of tABI-cc, tABI-power, and ECoG for the same rat (rat 14). First, it can be seen from Fig. 8 (a-c) that, with obvious strong signal observed at spot 17, consistent brain activation mappings are imaged with these three methods. Quantitatively, the correlation coefficient between tABI-cc and ECoG is 0.3824 ($p = 0.0642$). And the correlation coefficient between tABI-power and ECoG is 0.4240 ($p = 0.0795$). Besides, the normalized source density along the white line in Fig. 8 (a-c) is shown in Fig. 8 (d). For tABI-cc, tABI-power and ECoG, with the same peak position (y $= -$ 7mm), the anode width of the $-$6dB peak is 1mm, 2.57mm and 3.62mm respectively along the white line.

Under right eye steady-state visual stimulation paradigm, Fig. 9 shows the brain activation mappings of tABI-cc, tABI-power, and ECoG for the same rat (rat 15). First, it can be seen from Fig. 9 (a-c) that, with obvious strong signal observed at spot 14, consistent brain activation mappings are imaged with these three methods. Quantitatively, the correlation coefficient between tABI-cc and ECoG is 0.6636 ($p = 0.0027$) And the correlation coefficient between tABI-power and ECoG is 0.7527 ($p = 0.0549$). Besides, the normalized source density along the white line in Fig. 9 (a-c) is shown in Fig. 9 (d). For tABI-cc, tABI-power and ECoG, with the same peak position

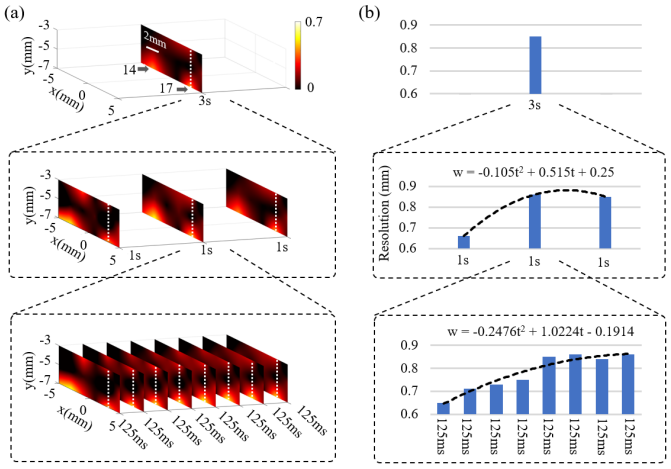

Fig. 10. (a) The tABI-cc images within 3s, 1s and 125ms obtained on same rat. (b) The resolution of the tABI-cc images: The width of the −6dB peak of the correlation coefficient at spot 17 along the white dashed-line.

(y = − 7mm), the anode width of the −6dB peak is 2.32mm, 2.53mm and 2.96mm respectively along the white line.

These experiment results validate both the tABI-cc and tABI-power can accurately map living rat brain activation under different steady-state visual stimulation paradigms. What's more, with transcranial measurement, tABI has millimeter-level (<3mm) spatial resolution.

D. tABI Transient Imaging

To evaluate the tABI potential for imaging transient brain activity, we implement tABI-cc in different time-scales for one rat (rat 13) under binocular steady-state visual stimulation paradigm. The correlation coefficient is directly adopted to image. The tABI-cc images of 3s, 1s and 125ms are respectively shown in Fig. 10 (a). At the three time-scales, consistent activation mappings are presented, with obvious strong signals observed at spot 14 and 17. In addition, Fig. 10 (b) shows the width variation of the −6dB peak at spot 17 along the white dashed-line. With 3s time-scale, the width of the −6dB peak is the average of 3-second state. With 1s time-scale, the widths of the −6dB peak are the corresponding average of 1-second state. And the width in the second second is significantly higher than that in the first second and is almost the same as the third second. With 125ms time-scale, the widths of the −6dB peak are shown in Fig. 10 (b), which are the corresponding average of 125-millisecond state. Quantitatively, the fitted equation for width w(mm) versus time t (s) is $w = -0.2476t^2 + 1.0224t - 0.1914$. Marked with the black curve in Fig. 10 (b), the fitting curve shows that the width of the −6dB peak increases before the fifth 125ms, and then tends to stabilize. Consistent with other neural recording experiments [26], these results show that the brain activation strength increases first and then tends to stabilize with the increase of visual stimulation time. In a word, these results validate tABI can accurately image brain activity at high temporal (125ms) resolution.

V. Discussion

In this study, we designed three visual stimulation paradigms to successfully activate different brain regions in the rat brain. And we demonstrate that tABI can accurately identify activation regions from both the time and frequency domains under three visual stimulation paradigms. Activated regions are further verified using ECoG. To make the experimental results more convincing, we first performed the tABI experiment and then the ECoG experiment in the same rat. Under the three visual stimulation paradigms, all three imaging methods showed activation in the same brain region under the same visual stimulation paradigm, and the spatial resolution of tABI in the in vivo rat experiment could be limited to 3mm. Finally, we explore the potential of tABI for transient imaging, demonstrating that the temporal resolution of tABI can reach 125ms.

Notably, we achieved localization of activated brain regions in rats under different visual stimulation paradigms using only one pair of electrodes. In addition, the electrode is a cylindrical electrode placed on the skull. Compared with the invasive 18-needle electrode imaging method, it avoids the pain of craniotomy in rats but can perform brain activation localization. This further affirms the brain imaging capabilities of tABI. In previous studies, it has been shown that appropriately increasing the number of electrodes and choosing an appropriate electrode layout can significantly improve the signal-to-noise ratio of images [21], [25]. We will try adding electrode arrays to improve the imaging quality of tABI in future work.

There are some possible limitations in this study. Firstly, due to the individual differences of rats, the activation areas of all rats are not completely consistent, especially with different paradigms. Therefore, when analyzing brain area signals of different experimental paradigms, the spots selected by the right eye stimulation paradigm are different from those of the other two paradigms. Besides, point-by-point scanning is adopted in the tABI experiment, which undoubtedly increases the acquisition time. In the future, we will improve the probe moving mode and ultrasound focusing mode to overcome these limitations. Finally, to accurately locate the positions of electrodes and FUS, the scalp is excised to reveal the skull. In the next work, MRI will be considered to adopt.

We used two tABI imaging modalities, tABI-cc, tABI-power. The spatial resolution of these two imaging modalities is limited by the focal field of the ultrasound probe, and the temporal resolution is limited by the frequency of the visual stimulus (8Hz). However, it is a challenge to form a small focal spot in the detected brain region and ensure biological safety after ultrasound penetrates the skull. The frequency of visual stimulation in this study is selected with reference to the research results of Peng Xu *et al.* [26], and 8Hz stimulus can evoke the strong SSVEP. In the next work, we will continue to optimize the scanning step size and visual stimulation frequency to further demonstrate the potential of tABI for high spatiotemporal resolution imaging in the living rat brain.

VI. Conclusion

In this study, in vivo tABI of different visual stimulation paradigms is first achieved. And tABI-cc, tABI-power can accurately locate the brain activation regions under different

visual stimulation paradigms. In addition, with transcranial measurement, tABI has millimeter-level spatial resolution (<3mm) and millisecond-level temporal resolution (125ms). This study proves the imaging potential of tABI, and tABI is expected to develop into a brain imaging technology with high temporal and spatial resolution.

REFERENCES

[1] J. R. Polimeni, B. Fischl, D. N. Greve, and L. L. Wald, "Laminar analysis of 7T BOLD using an imposed spatial activation pattern in human V1," *NeuroImage*, vol. 52, no. 4, pp. 1334–1346, Oct. 2010.

[2] B. A. Ardekani *et al.*, "Functional magnetic resonance imaging of brain activity in the visual oddball task," *Cognit. Brain Res.*, vol. 14, no. 3, pp. 347–356, Nov. 2002.

[3] J. Grinband, J. Steffener, Q. R. Razlighi, and Y. Stern, "BOLD neurovascular coupling does not change significantly with normal aging," *Hum. Brain Mapping*, vol. 38, no. 7, pp. 3538–3551, Apr. 2017.

[4] G. Lioi *et al.*, "Simultaneous EEG-fMRI during a neurofeedback task, a brain imaging dataset for multimodal data integration," *Sci. Data*, vol. 7, no. 1, p. 173, Jun. 2020.

[5] Y. J. Zhou *et al.*, "Research progress of multimodal functional neural imaging technology based on EEG," *Chin. J. Biomed. Eng.*, vol. 39, no. 5, pp. 595–602, Oct. 2020.

[6] Y. Qin, P. Ingram, Z. Xu, M. O'Donnell, and R. S. Witte, "Performance of a transcranial U.S. array designed for 4D acoustoelectric brain imaging in humans," in *Proc. IEEE Int. Ultrason. Symp. (IUS)*, Washington, DC, USA, Sep. 2017, pp. 1–4.

[7] F. E. Fox, K. F. Herzfeld, and G. D. Rock, "The effect of ultrasonic waves on the conductivity of salt solutions," *Phys. Rev.*, vol. 70, nos. 5–6, pp. 329–339, 1946.

[8] J. Jossinet, B. Lavandier, and D. Cathignol, "The phenomenology of acousto-electric interaction signals in aqueous solutions of electrolytes," *Ultrasonics*, vol. 36, nos. 1–5, pp. 607–613, 1998.

[9] B. Lavandier, J. Jossinet, and D. Cathignol, "Experimental measurement of the acousto-electric interaction signal in saline solution," *Ultrasonics*, vol. 38, no. 9, pp. 929–936, 2000.

[10] R. Olafsson, R. S. Witte, S.-W. Huang, and M. O'Donnell, "Ultrasound current source density imaging," *IEEE Trans. Biomed. Eng.*, vol. 55, no. 7, pp. 1840–1848, Jul. 2008.

[11] Y. Zhou, X. Song, Z. Wang, F. He, and D. Ming, "Multisource acoustoelectric imaging with different current source features," *IEEE Trans. Instrum. Meas.*, vol. 70, pp. 1–9, 2021.

[12] R. Witte, R. Olafsson, S.-W. Huang, and M. O'Donnell, "Imaging current flow in lobster nerve cord using the acoustoelectric effect," *Appl. Phys. Lett.*, vol. 90, no. 16, Apr. 2007, Art. no. 163902.

[13] Y. Qin, Q. Li, P. Ingram, C. Barber, Z. Liu, and R. S. Witte, "Ultrasound current source density imaging of the cardiac activation wave using a clinical cardiac catheter," *IEEE Trans. Biomed. Eng.*, vol. 62, no. 1, pp. 241–247, Jan. 2015.

[14] B. Berthon *et al.*, "Mapping biological current densities with ultrafast acoustoelectric imaging: Application to the beating rat heart," *IEEE Trans. Med. Imag.*, vol. 38, no. 8, pp. 1852–1857, Aug. 2019.

[15] A. Alexander *et al.*, "*In vivo* acoustoelectric imaging for high-resolution visualization of cardiac electric spatiotemporal dynamics," *Appl. Opt.*, vol. 59, no. 36, pp. 11292–11300, Dec. 2020.

[16] B. He, "Focused ultrasound help realize high spatiotemporal brain imaging?—A Concept on acousto-electrophysiological neuroimaging," *IEEE Trans. Biomed. Eng.*, vol. 63, no. 12, pp. 2654–2656, Dec. 2016.

[17] A. Burton, C. A. Wilhite, T. K. Bera, P. Ingram, S. L. Cowen, and R. S. Witte, "Development of a mobile platform for acoustoelectric brain imaging in rats," in *Proc. IEEE Int. Ultrason. Symp. (IUS)*, Kobe, Japan, Oct. 2018, pp. 1–4.

[18] C. Preston, W. S. Kasoff, and R. S. Witte, "Selective mapping of deep brain stimulation lead currents using acoustoelectric imaging," *Ultrasound Med. Biol.*, vol. 44, no. 11, pp. 2345–2357, Nov. 2018.

[19] A. Barragan, C. Preston, A. Alvarez, C. P. Ingram, T. Kanti Bera, and R. S. Witte, "4D transcranial acoustoelectric imaging of current densities in a human head phantom," in *Proc. IEEE Int. Ultrason. Symp. (IUS)*, Oct. 2019, pp. 2049–2051.

[20] C. Preston, A. M. Alvarez, A. Barragan, J. Becker, W. S. Kasoff, and R. S. Witte, "High resolution transcranial acoustoelectric imaging of current densities from a directional deep brain stimulator," *J. Neural Eng.*, vol. 17, no. 1, Feb. 2020, Art. no. 016074.

[21] A. Barragan *et al.*, "Acoustoelectric imaging of deep dipoles in a human head phantom for guiding treatment of epilepsy," *J. Neural Eng.*, vol. 17, no. 5, Oct. 2020, Art. no. 056040.

[22] X. Song, X. Chen, J. Guo, M. Xu, and D. Ming, "Living rat SSVEP mapping with acoustoelectric brain imaging," *IEEE Trans. Biomed. Eng.*, vol. 69, no. 1, pp. 75–82, Jan. 2022.

[23] G. Paxinos and C. Watson, *The Rat Brain in Stereotaxic Coordinates*, 6th ed. New York, NY, USA: Academic, 2007.

[24] N. J. Priebe and A. W. McGee, "Mouse vision as a gateway for understanding how experience shapes neural circuits," *Frontiers Neural Circuits*, vol. 8, p. 123, Oct. 2014.

[25] X. Song, G. Han, Y. Zhou, M. Xu, M. Liu, and D. Ming, "A symmetrical sensor configuration for acoustoelectric brain imaging," *IEEE Sensors J.*, vol. 21, no. 20, pp. 22891–22898, Oct. 2021.

[26] P. Xu *et al.*, "Cortical network properties revealed by SSVEP in anesthetized rats," *Sci. Rep.*, vol. 3, no. 1, p. 2496, Aug. 2013.